

Early Jurassic large igneous province carbon emissions constrained by sedimentary mercury

Received: 6 June 2023

Accepted: 19 January 2024

Published online: 26 February 2024

 Check for updates

Isabel M. Fendley^{1,2}✉, Joost Frieling¹, Tamsin A. Mather¹, Micha Ruhl³, Stephen P. Hesselbo⁴ & Hugh C. Jenkyns¹

Large igneous province eruptions and their carbon emissions often coincide with, and are hypothesized to have driven, severe environmental perturbations in the geological past. However, the vast scale of large igneous provinces and uncertainties in magmatic volatile contents and radioisotopic dates limit our ability to resolve gas emissions in detail over time. Here we employ high-resolution (~5–200 kyr) sedimentary mercury data from the Llanbedr (Mochras Farm) borehole, Wales, to derive quantitative large igneous province degassing estimates over a 20-million-year-long Early Jurassic interval (195–175 million years ago). Intervals of relatively elevated sedimentary mercury coincide with episodes of carbon-cycle change, including the Toarcian Oceanic Anoxic Event (183–182 million years ago). We use excess mercury loading to estimate large igneous province-associated carbon emissions, revealing that multi-millennial episodes of activity plausibly drove recognized p_{CO_2} and temperature increases. However, previous carbon-cycle model-based carbon emission scenarios require faster and larger carbon inputs than our proposed emissions. Resolving this discrepancy may require climate–carbon-cycle feedbacks or co-emitted gases to substantially exacerbate the carbon-cycle response, processes potentially underestimated in current models. Our long and near-continuous record of Early Jurassic large igneous province activity demonstrates mercury’s potential as a tool to resolve past carbon fluxes.

The emplacement of large igneous provinces (LIPs), the largest known volcanic events in Earth’s history, is commonly associated with severe environmental, climatic and ecosystem disturbance, including mass extinctions and oceanic anoxic events¹. LIP-associated carbon emissions (primarily magmatic and thermogenic CO_2) are hypothesized to have driven climate change, ocean acidification and anoxia–euxinia¹.

Although the conceptual framework for the Earth system effects of LIP carbon emissions is well established (Fig. 1), understanding these processes quantitatively remains a major challenge. The quantity and timing of LIP-associated gas emissions are usually estimated from geochronology on LIP materials and geochemical indicators of volatile content in the lavas (and affected country rocks)^{2–4}. Several factors limit

¹Department of Earth Sciences, University of Oxford, Oxford, UK. ²Department of Geoscience, Pennsylvania State University, University Park, PA, USA.

³Department of Geology and SFI Research Centre in Applied Geosciences (iCRAG), Trinity College Dublin, the University of Dublin, Dublin, Ireland.

⁴Camborne School of Mines, Department of Earth and Environmental Sciences, University of Exeter, Penryn Campus, Penryn, UK.

✉e-mail: ifendley@psu.edu

this approach: (1) current maximum level of precision for radioisotopic dating techniques (for example, 10s–100s of kiloyears for Jurassic igneous material^{2,5,6}); (2) difficulty translating radioisotopic dates into volumetric emplacement rates through time, given the spatiotemporal complexity of LIPs^{5,7}; (3) the unreliability of geochemical indicators of degassing in these ancient rocks, especially for carbon⁸. Thus, direct sampling of LIP materials alone cannot currently provide continuous sub-10 kyr emission data as required to link LIP activity quantitatively and mechanistically to climatic and carbon-cycle perturbations in detail.

As an alternative, carbon-cycle models have been used to estimate the total carbon emissions required to reproduce palaeoenvironmental records (for example, $\delta^{13}\text{C}$, temperature, pH and p_{CO_2})^{9,10}. This approach generally assumes that LIP-associated carbon emissions were entirely responsible for the observed perturbations and that carbon-cycle models adequately capture the Earth system response during the geological past. In such studies, LIP emission histories and feedback systems are not independently constrained, challenging our ability to test and validate our understanding of Earth system responses to large volcanic carbon emissions using palaeoclimatic reconstructions alone. For example, these Earth system responses include a number of both positive and negative feedbacks, such as amplification by perturbing exogenic carbon reservoirs (clathrates, terrestrial carbon reservoirs)^{10–12} and dampening via increased silicate weathering and organic-carbon burial^{13,14}, which are incorporated into carbon-cycle models using differing parameterizations and mathematical simplifications. Independent carbon emissions estimates are required to assess whether carbon-cycle models sufficiently capture the full spectrum of Earth system sensitivity. Sedimentary mercury (Hg) concentration has been used as a qualitative indicator of large-scale volcanic activity during the geological past¹⁵ as volcanism is a primary natural source of Hg to the environment¹⁶. In this work, we use a chronologically well-constrained and high-resolution record to develop a sedimentary Hg-based quantitative proxy for LIP-associated (magmatic and thermogenic) gas emissions that aims to address this critical challenge.

The Early Jurassic period (201–175 million years ago (Ma)) witnessed a complex series of changes in climate, ocean chemistry, sea level and ecological diversity and included the emplacement of two LIPs: the Karoo–Ferrar LIP (KFLIP) and late-stage (post-Triassic) activity of the Central Atlantic magmatic province (CAMP^{6,17}). The Toarcian Oceanic Anoxic Event (T-OAE), coeval within dating uncertainty with the KFLIP main phase, was among the most severe Mesozoic palaeoenvironmental events^{2,18}. The T-OAE was characterized by global climate warming, regional oceanic anoxia–euxinia, ocean acidification, mass extinction and a major carbon-cycle perturbation¹⁸. In addition to the T-OAE, the Early Jurassic also contains a comparatively long-term (~5 Myr) negative carbon-isotope excursion (n-CIE) centred around the Sinemurian–Pliensbachian (S–P) stage boundary, hypothesized as related to late-stage CAMP volcanism¹⁹, and complex changes in $\delta^{13}\text{C}$ in the latest Pliensbachian²⁰.

While the overall temporal relationship between the main phase of KFLIP magmatism and the T-OAE is reasonably well established, the quantity of coeval LIP-associated carbon emissions is poorly constrained^{9,10}. In addition, whether LIP eruptions coincided with other Early Jurassic CIEs remains far less certain, and whether a more general mechanistic relationship exists between environmental events during the Early Jurassic and LIP volcanism remains to be resolved^{19–21}.

In this work, we present a compilation of new and literature sedimentary Hg concentration data from the Llanbedr (Mochras Farm) borehole, Wales, UK, creating an unprecedentedly long and high-resolution record spanning the Late Sinemurian age (~196 Ma) through the Late Toarcian age (176 Ma). This allows us to explore whether large-scale volcanism temporally coincides with the Early Jurassic CIEs. Further, we combine the data with knowledge of global Hg cycling and Hg/CO₂ relationships for present-day volcanism to

estimate excess LIP-associated carbon (CO₂) emissions spanning the entire 20 Myr record. Focusing on the T-OAE, we use these emissions estimates to test whether current model scenarios adequately represent the environmental response to LIP-associated (magmatic and thermogenic) carbon emissions and feedback processes.

Geological setting

The Llanbedr (Mochras Farm) borehole²² (hereafter termed Mochras) in the Cardigan Bay Basin, Wales, offers one of the most stratigraphically expanded records of the hemipelagic Lower Jurassic. The Cardigan Bay Basin was within the Laurasian seaway, which connected the Arctic Sea and Tethys Ocean²³ (Fig. 1). The timing of key events within the Mochras record is constrained via ammonite and foraminiferal biostratigraphy, astrochronology and $\delta^{13}\text{C}$ chemostratigraphy^{12,19,24–26}. There are no major hiatuses within the Lower Jurassic section²⁵, and carbon-, oxygen- and osmium-isotope trends at Mochras are similar to those from Tethyan localities, suggesting regular seawater exchange with the global ocean^{12,27,28}.

Lower Jurassic (Sinemurian–Toarcian) sedimentary Hg record

Volcanic systems emit mercury gas during eruptive and non-eruptive degassing, including intrusive magmatic activity²⁹. Indeed, large-scale and prolonged subaerial volcanism^{30,31} can be traced by sedimentary Hg concentrations in the geological record: increases in Hg have been found to occur coeval with, for example, the main-phase eruptive intervals of the KFLIP^{30,32–34} and CAMP¹⁷.

Our new Hg data span the last ~2 Myr of the Sinemurian and the entire Pliensbachian, substantially extending the existing Mochras Hg data for the uppermost Pliensbachian and Toarcian^{27,30,34}. We investigate the changes in Hg deposition through time as a reflection of the variable availability of environmental Hg and, hence, notable changes in large-scale global volcanic activity (probably dominantly LIP related).

As host phase complexity³¹ can influence the interpretation of sedimentary Hg records, we quantitatively account for related processes before using the Mochras record to estimate LIP-associated emissions. Although a simple ratio (Hg/total organic carbon (TOC)) is typically used for this purpose, this does not always fully correct for host-phase biases, nor does it quantify the additional environmental Hg present over background levels during periods of sedimentary Hg enhancement³¹. Instead, we developed a quantitative framework based on an empirical assessment of co-variation between Hg concentration and that of host phases (for example, TOC and S) and dilution effects due to sedimentary CaCO₃—each statistically significant in the Mochras dataset (Supplementary Information 1.2). The framework relies on the observation that Hg behaves consistently throughout our dataset. Residual Hg (Hg_R) is found here by first calculating Hg and TOC concentrations on a CaCO₃-free basis for each sample and then adopting a best-fit curve between them for the whole dataset. Hg_R is the difference between each sample's CaCO₃-free Hg concentration and the obtained best-fit curve (Methods and Supplementary Information 1.2). We expect this adaptable framework to be widely applicable as it can accommodate a range of Hg-host phase relationships, including, but not limited to, a linear relationship.

Hg_R hence represents the excess Hg loading beyond what is expected given the geochemistry of each sample. We use scaling factors from Hg-cycle box-model results^{35,36} to determine the increased atmospheric Hg flux associated with elevated Hg_R (Fig. 2 and Supplementary Information 4). The Hg-cycle model explicitly considers the critical effects of biogeochemical recycling of Hg within and between terrestrial and marine reservoirs before deposition in sediments. This is important because terrestrial sediments and organic material are major Hg sources to modern and Jurassic near-shore marine environments^{35,37}. We compare the Mochras core dataset with the coastal

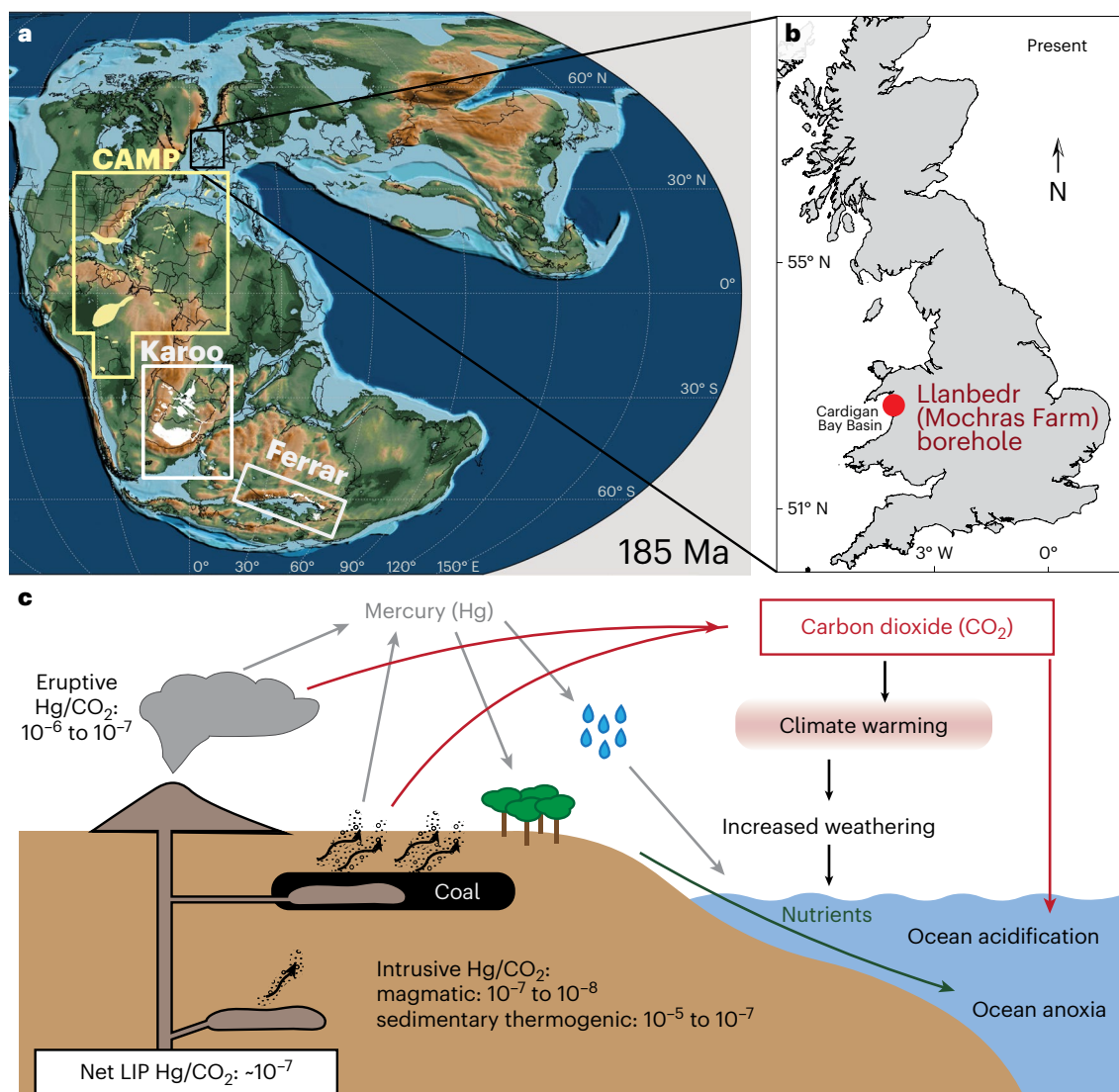


Fig. 1 | Maps and illustration of LIP gas emissions processes and environmental effects. **a**, Palaeogeographic reconstruction²³ showing the Jurassic location of the Mochras borehole and locations of CAMP and KFLIP based on modern outcrop extent (approximate locations shown via yellow and white boxes/shading, respectively); primary outcrop locations for the KFLIP include present-day Africa (Karoo): South Africa, Lesotho, Namibia, Botswana, Mozambique, Zimbabwe and Zambia; Antarctica: Dronning Maud Land (Karoo) and Dry Valleys (Ferrar), and Tasmania (Ferrar)^{5,6,43}. **b**, Inset map showing the

present-day location of the Mochras borehole³². **c**, Illustration of direct and indirect feedback effects of LIP-associated CO₂ emissions¹ and simplified LIP Hg emissions pathways. Typical Hg/CO₂ ratios are shown for each volatile source (eruptive, intrusive magmatic and intrusive thermogenic), and an approximate net LIP-associated Hg/CO₂ value (Methods, Supplementary Information 4 and Supplementary Table 1; thermogenic sources are based on theoretical calculations and using natural (in situ) coal fires as an analogue). Basemap in **a** adapted with permission from ref. 23, Annual Reviews.

marine sediment box as this locality received substantial amounts of terrigenous material²⁶.

We expect the primary control on Hg_R to be subaerial volcanic-associated gas emissions as submarine Hg emissions have limited geographical reach³⁸. Although processes other than volcanism (including wildfires, enhanced weathering and redox changes) may result in excess Hg deposition, they are unlikely to have substantively affected our dataset (Supplementary Information 2). We therefore consider our data a representative estimate of subaerial Hg emissions in this instance, probably dominated by the volcanic-associated flux (Fig. 2).

Relationship between LIP activity and carbon-cycle events

We assess the relationship between LIP volcanism and carbon-cycle changes by comparing the Hg_R record and carbon-isotope stratigraphy in the Mochras core (Fig. 2). We find that the Sinemurian–Pliensbachian

(S–P) transition, the upper *margaritatus* Zone, the Pliensbachian/Toarcian boundary and the T-OAE n-CIE each coincide with increases in residual sedimentary Hg levels above background (95%) variability (Fig. 2), albeit with different magnitudes. Thus, an increase in global volcanic-related (LIP) Hg emissions appears to have temporally coincided with all four n-CIEs.

To test whether a volcanic CIE driver is plausible, we use Hg_R to estimate the quantity of coincident LIP-associated carbon emissions. Measurements at present-day volcanoes, experiments and estimates of thermogenic emissions suggest that Hg and carbon emissions are closely coupled under most extrusive and intrusive volcanic scenarios²⁹. Thus, using modern-analogue Hg/CO₂ gas ratios from volcanism and sediment combustion, we estimate the carbon (CO₂) emissions that probably corresponded with the excess Hg fluxes (Figs. 1 and 3, Methods, Supplementary Information 4 and Supplementary Table 1). To estimate the consequent increase in exogenic carbon reservoirs,

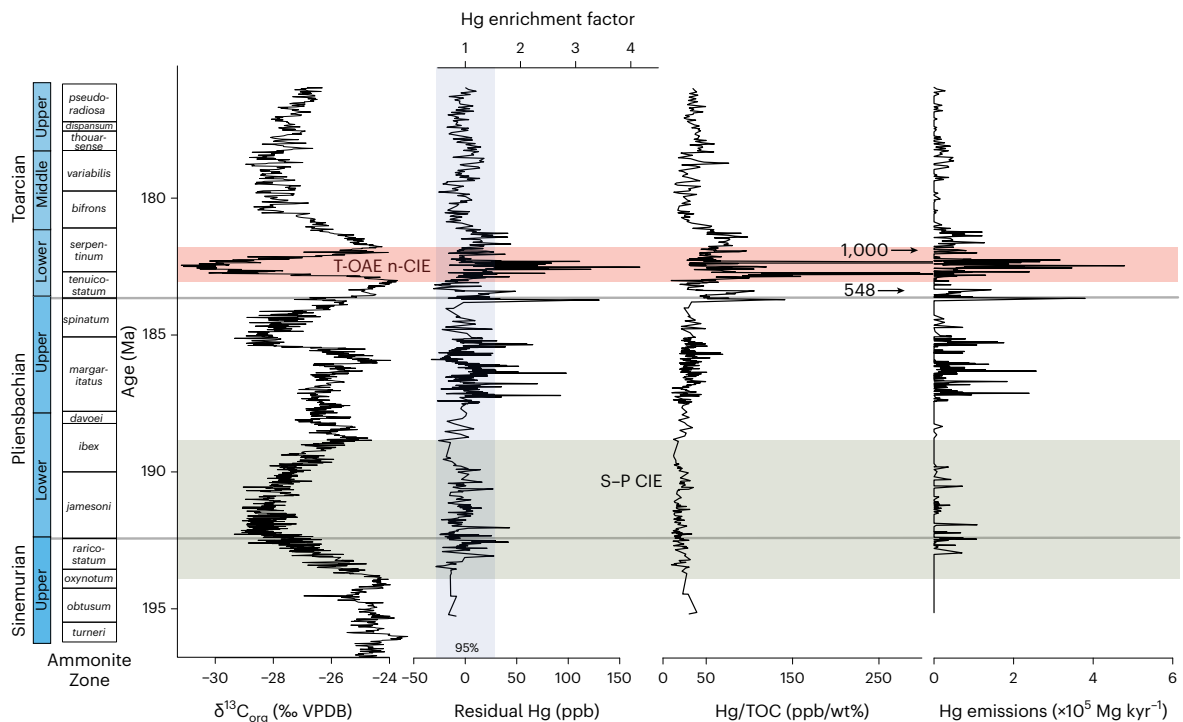


Fig. 2 | Mercury-derived datasets, ammonite biostratigraphy and organic-carbon isotopic composition for the Mochras core versus age. Hg datasets (Supplementary Information 7)^{12,24,46,47}; left plot shows residual Hg (Hg_R , $ng\ g^{-1}$, ppb) and Hg enrichment (unitless) (Supplementary Information 1 and 3) with the blue shaded box indicating background (95%) Hg variability; middle plot shows Hg/TOC (in ppb/wt%) for comparison; right plot shows Hg emissions ($Mg\ kyr^{-1}$) calculated from residual Hg using scaling factors from a Hg-cycle box model (Supplementary Information 4)^{35,36}. Hg enrichment is Hg_R divided

by the corresponding value on the calcium carbonate-free Hg versus calcium carbonate-free TOC best-fit curve. The slope of this curve is very shallow for our data (Supplementary Information 1.3 and Supplementary Fig. 6) and hence is nearly equivalent to dividing by a constant, enabling a secondary axis for approximate enrichment factor on the residual Hg plot. The S-P and T-OAE carbon-isotope excursions are labelled and indicated via green and red shading, respectively. $\delta^{13}C_{org}$, organic-carbon isotopic composition; VPDB, Vienna Pee Dee Belemnite.

we use a 300 kyr rolling window sum to approximate C accumulation before removal via weathering/burial¹³ and to calculate the corresponding resultant value of atmospheric p_{CO_2} (ref. 39). We compare our carbon outgassing estimates with emission scenarios used in carbon-cycle model studies of the T-OAE interval (Fig. 4).

Volcanism at the Sinemurian–Pliensbachian transition?

The 5 Myr duration, 3–4‰ (ref. 12) S–P boundary n-CIE in Mochras $\delta^{13}C_{org}$ has previously been attributed to volcanic-associated CO_2 emissions. However, the evidence for substantial LIP volcanism during this interval is sparse⁶ (Supplementary Information 5), and there is no conclusive geochronological or volcanological evidence of a large, sustained episode of volcanic activity/degassing across the S–P boundary as required to explain the long-duration n-CIE⁴⁰.

The upper Sinemurian through lower Pliensbachian (~1,300–1,000 m core depth, ~195–188 Ma) generally shows background residual Hg concentrations. We propose that the few Hg_R outliers close to the S–P boundary (Fig. 2) correspond to a modest increase in volcanic-associated CO_2 emissions between 194 and 190 Ma, estimated as cumulative ~2,420 PgC emitted over this 4 Myr period (Hg/CO_2 of 10^{-7}). Due to the extended duration and coeval carbon removal via negative feedbacks (for example, silicate weathering), a modest accumulation of 625 PgC is estimated for the ocean–atmosphere carbon pool (Fig. 3), much less than required to drive a 3–4‰ n-CIE⁴⁰.

As submarine LIP volcanism generally leaves only regional sedimentary Hg signals³⁸, we cannot exclude that submarine volcanic activity and carbon emissions played a role while leaving only the few Hg peaks recorded in the Mochras core. Although volcanic forcing cannot be excluded, our new Hg data do not support subaerial

volcanism as the primary driver, and the ultimate cause of the S–P n-CIE remains enigmatic.

Late Pliensbachian volcanism

In contrast to the clear n-CIEs associated with the T-OAE and S–P, carbon-isotope records for the late Pliensbachian show spatially heterogeneous trends, which have previously been attributed to erosive sea-level fall in the latest Pliensbachian²⁰. The Mochras record, considered among the more complete successions for this interval, shows an abrupt negative CIE at the *margaritatus/spinatum* zonal boundary, superimposed onto a positive trend, and a subsequent smaller n-CIE at the Pliensbachian/Toarcian boundary^{12,20}. Previous studies have variably linked the n-CIEs to a combination of KFLIP volcanism and orbitally forced climate change^{20,21,30}.

The upper Pliensbachian and Toarcian (1,000–700 m core depth, ~188–180 Ma) interval has several Hg_R peaks (100–200 ppb) starting in the *margaritatus* Zone and persisting through the lower Toarcian. This is consistent with existing Hg records from Switzerland, Dorset (UK) and Chile, which have Hg and Hg/TOC peaks within the *margaritatus* Zone^{33,41}. Overall, these results strongly suggest that enhanced (LIP) volcanism occurred around this time. Both n-CIEs are coeval with Hg_R increases; however, other Hg_R peaks are not associated with notable changes in $\delta^{13}C_{org}$. This complexity may be explained via variability in the $\delta^{13}C$ of LIP-associated carbon emissions (for example, magmatic ~5‰ versus thermogenic < ~20‰) or variations in the global C cycle in response to volcanic-related (or other) forcings.

The Hg_R peaks in the *margaritatus* Zone and the Pliensbachian/Toarcian boundary each correspond to a predicted exogenic carbon increase of up to 3,000 Pg (Fig. 3). The calculated increase in p_{CO_2} is ~300–375 ppm (initial p_{CO_2} of 500–1,000 ppm), consistent with a

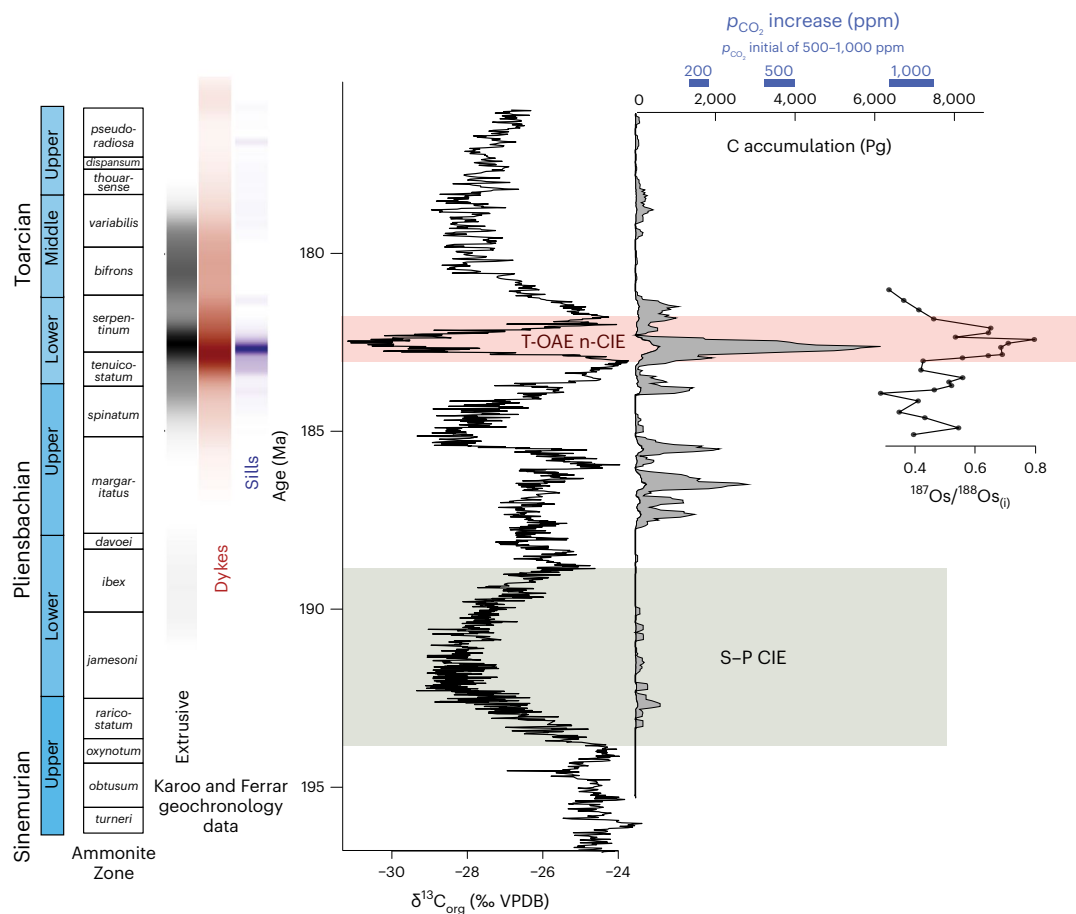


Fig. 3 | Karoo and Ferrar geochronology data, with organic-carbon-isotope record, mercury-derived carbon accumulation estimates and osmium-isotope data (all from the Mochras core). The largest estimated carbon accumulation coincides with the T-OAE n-CIE^{12,24} and an increase in weathering demonstrated by a shift towards radiogenic osmium-isotope values²⁷. Compilations of Karoo and Ferrar radioisotopic dates⁶ of extrusive lavas, dykes and sills are plotted as coloured bars that are kernel density diagrams (stronger colouration represents higher probability density). The uncertainty on these dates was incorporated by bootstrap resampling each date 100 times and plotting the distribution of the total results. Estimated carbon accumulation (Pg) was calculated by summing carbon emissions over a 300 kyr moving window to account for carbon accumulation in the ocean–atmosphere system, the decay

timescale of which is determined by negative feedbacks¹³. Carbon emissions are a scaling of Hg emissions (Fig. 2), with a grey region spanning Hg/CO₂ ratios between 10⁻⁶ as a minimum and 10⁻⁷ as a most likely net composition of LIP-associated emissions (Fig. 1). To contextualize the carbon accumulation, an equivalent resulting *p*CO₂ estimate, assuming an initial *p*CO₂ of 500–1,000 ppm, is included on the axis label. This *p*CO₂ increase is calculated using equilibrium ocean carbonate chemistry partitioning of CO₂, between ocean and atmosphere as a function of *p*CO₂ (three-box model)³⁹ (Methods and Supplementary Information 4). *p*CO₂ increase is used as a metric of carbon-cycle influence, rather than the amplitude of potential (n)-CIE, as these carbon emissions estimates are agnostic to the proportion from magmatic versus thermogenic sources, and hence the net δ¹³C value^{12,24} of the emissions is undetermined.

boron-isotope-based *p*CO₂ record from the uppermost *margaritatus* Zone⁴², and probably resulted in climate warming and environmental change. Although the *margaritatus* Zone and the Pliensbachian/Toarcian boundary precede the main phase of KFLIP, they are within the known temporal range of early KFLIP intrusive activity⁵ (and, for note, the first stage of Chon Aike silicic LIP-style volcanism in Antarctica from 189 to 183 Ma (ref. 43); there are, however, substantial unknowns regarding Hg and carbon emissions from silicic LIP-style episodes, and thus we do not consider this further here). The magnitude of the Hg_r peaks and corresponding carbon emissions suggest that volcanic activity may be implicated in the late Pliensbachian environmental change.

T-OAE and C-cycle implications

The largest peaks in Hg_r, and hence largest potential CO₂ emissions, of the entire 20 Myr record occur within the interval of the T-OAE n-CIE (Figs. 2 and 3), consistent with previous studies that documented elevated Hg concentrations at the Pliensbachian/Toarcian boundary and across the T-OAE interval^{30,32,33,37}. The relative magnitude of these peaks

compared with the rest of the Hg_r record suggests that KFLIP-associated gas emissions were greatest during this part of the Early Jurassic^{30,32}.

We estimate that the Hg_r peaks during the T-OAE n-CIE corresponded with considerable CO₂ emissions (a total of ~17,000 PgC emitted during the main phase of KFLIP, 184–181 Ma) and a maximum total accumulation of ~6,200 PgC, doubling to tripling atmospheric *p*CO₂—consistent with stomatal and boron-isotope-based estimates^{42,44}. The timing of maximum Hg-based carbon emissions is consistent with geochronology from the KFLIP (Fig. 3), which suggests that the majority of KFLIP volcanism, both intrusive and extrusive activity, coincided with the T-OAE at 183–182 Ma (refs. 2, 6).

We compare estimated carbon emitted during the T-OAE n-CIE (KFLIP main phase) between 183 and 182 Ma with independent total carbon and average emission rate estimates from LIP-volcanology-based proxies (for example, melt inclusions, igneous geochemistry and modelling of magmatic processes) for several other LIPs⁴⁵ (Fig. 4). Although the time history of gas emissions found using these proxies has inherent limitations due to uncertainty in volcanic stratigraphy, geochronology and gas content, the total summed carbon emissions reflect what is

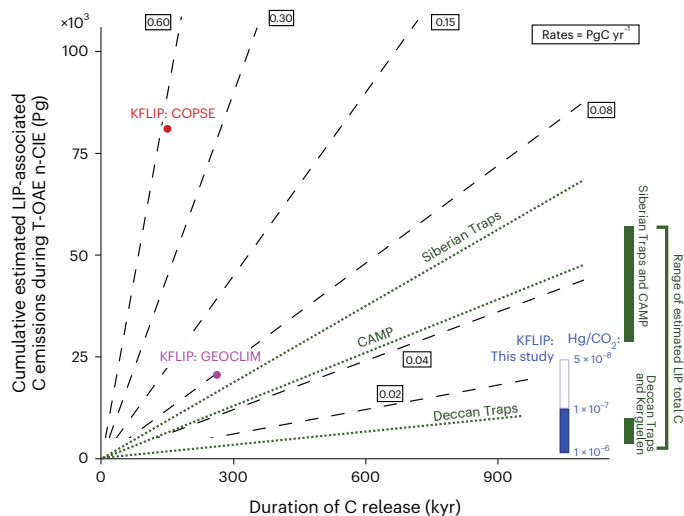


Fig. 4 | Mercury-based carbon emissions estimates across the T-OAE n-CIE compared with literature estimates for the Karoo–Ferrar LIP and other LIPs. Literature carbon-cycle model-based estimates of total KFLIP carbon emissions across the T-OAE n-CIE based on GEOCLIM⁹ (purple point) and COPSE¹⁰ (red point) model scenarios matching $\delta^{13}\text{C}$, p_{CO_2} and temperature proxy data with carbon emissions estimates for several other LIPs (green bars on the right of the plot represent the total emissions quantity; dotted lines are average emission rates in units of Pg yr^{-1}). KFLIP model scenarios incorporate carbon fluxes with $\delta^{13}\text{C}$ values indicative of a combination of CO_2 and CH_4 (Supplementary Information 4.4). Total carbon emissions and durations are compared to best represent an integrated view of the T-OAE, less dependent on sampling resolution and age models. Hg-based carbon estimates: the blue bar represents the range of carbon emissions estimated for Hg/ CO_2 ratios between 10^{-6} and 10^{-7} during the T-OAE n-CIE (wherein CO_2 emissions and n-CIE durations are equivalent). A Hg/ CO_2 ratio of 10^{-7} is hypothesized to be the most likely long-term net value, consistent with a combination of eruptive and diffusive (magmatic and thermogenic) degassing (Fig. 3). A Hg/ CO_2 ratio of 5×10^{-8} is shown to illustrate the maximum possible CO_2 emissions that may occur in specific diffusive degassing scenarios⁵³, although it is unlikely to represent a long-term net composition. Other LIP carbon emissions from a literature compilation^{3,45,54}: the green bars on the right of the plot represent LIP-proxy-based estimates of the quantity of total carbon emissions for several other LIPs (based on a combination of CO_2 content estimates, from melt inclusions and geochemical ratios, and thermogenic emissions estimates, and total LIP volumes), and the green dotted lines represent the average rate of carbon emission for those LIPs (based on the total quantity and the estimated emplacement duration). The Siberian Traps and CAMP represent LIPs with substantial associated thermogenic carbon emissions, and the Deccan Traps and Kerguelen Plateau represent LIPs with minimal thermogenic carbon emissions.

expected on the basis of our knowledge of LIP magmatic processes. Our Hg-based carbon quantity and rate estimates are somewhat higher than the ranges obtained for the Deccan Traps/Kerguelen Plateau but are smaller than those associated with the Siberian Traps/CAMP (Fig. 4).

Notably, we find that existing modelled LIP emission scenarios based on matching carbon-cycle model output with $\delta^{13}\text{C}$, temperature and/or p_{CO_2} proxy data require higher average carbon input rates and total amounts of carbon across the T-OAE than supported by our emissions estimates and existing estimates based on LIP-volcanology-based proxies (Fig. 4). We compare average emissions rates as they are less sensitive to sampling resolution and age model (Supplementary Information 4.4). We estimate that a total of $\sim 12,000 \text{ PgC}$ was released (Hg/ CO_2 of 10^{-7}) during the entire T-OAE n-CIE interval ($\sim 1 \text{ Myr}$), compared with estimates of $20,500 \text{ Pg}$ over 262 kyr and $81,000 \text{ Pg}$ over 150 kyr using published GEOCLIM⁹ and COPSE¹⁰ model results, respectively. Our most likely scenario, with Hg/ CO_2 by mass of 10^{-7} (a combination of eruptive and intrusive degassing, both magmatic and thermogenic; Fig. 1 and Supplementary Information 4.2), implies

average excess carbon input rates across the T-OAE of 0.012 Pg yr^{-1} (0.015 Pg yr^{-1} during the falling limb of the n-CIE; Supplementary Information 4.4), with an upper estimate of 0.023 Pg yr^{-1} (Hg/ CO_2 of 5×10^{-8}), compared with 0.08 and 0.54 Pg yr^{-1} for the GEOCLIM and COPSE scenarios, respectively. In addition, the duration of the T-OAE n-CIE using our updated Mochras age model is longer than in the GEOCLIM and COPSE model scenarios ($\sim 1 \text{ Myr}$ in our record versus $\sim 500 \text{ kyr}$; Fig. 4 and Supplementary Information 3). This difference has been noted in other records due to the choice of astronomical cycles⁴⁶, but recent U–Pb dates (which we incorporate) support the longer duration⁴⁷ (Supplementary Information 3). If a longer-duration n-CIE were modelled, more carbon input would be required to match the observed CIE amplitude. Alternatively, a shorter-duration T-OAE would require smaller Hg emissions to produce the observed Hg enrichment (given less dilution of the Hg emissions over time; Supplementary Information 4.1), similarly exacerbating the mismatch in carbon emission scenarios.

The discrepancies between our Hg-based estimates and the two carbon-cycle model scenarios suggest that our understanding of the early Jurassic carbon cycle is incomplete. Recent studies show that slow, state-dependent, positive-feedback processes leading to high Earth system sensitivity (for example, clay mineral formation⁴⁸, oxidative weathering⁴⁹, ocean circulation⁴⁹ and biological productivity⁵⁰) may be important factors. Both the complex feedback response to environmental change and the Early Jurassic background state (for example, the size of the initial exogenic carbon reservoir and weathering/erosional fluxes^{49,51}) may not be adequately included in model studies. In addition, this discrepancy raises the question of whether the role of other co-emitted gases (for example, SO_2 and CH_4), which are not included in our Hg-based estimates or most carbon-cycle/climate studies, should be specifically considered in the climate response to LIPs.

Our results demonstrate the utility of combining Hg records with Hg box models to provide quantitative LIP-associated Hg and carbon emissions estimates. This approach provides important constraints on LIP-associated gas emissions at a resolution relevant for palaeoclimate studies and thus can be used to diagnose Earth system processes insufficiently captured within models or the need to investigate alternative carbon sources. The framework we describe here can be applied to other Phanerozoic LIPs, providing that long-term, high-resolution and chronologically and geochemically well-constrained Hg records are available. We envisage that this methodology will improve our understanding of how LIP emplacement and other large carbon emission events affect the Earth system.

Online content

Any methods, additional references, Nature Portfolio reporting summaries, source data, extended data, supplementary information, acknowledgements, peer review information; details of author contributions and competing interests; and statements of data and code availability are available at <https://doi.org/10.1038/s41561-024-01378-5>.

References

- Clapham, M. E. & Renne, P. R. Flood basalts and mass extinctions. *Annu. Rev. Earth Planet. Sci.* **47**, 275–303 (2019).
- Burgess, S. D., Bowring, S. A., Fleming, T. H. & Elliot, D. H. High-precision geochronology links the Ferrar large igneous province with early-Jurassic ocean anoxia and biotic crisis. *Earth Planet. Sci. Lett.* **415**, 90–99 (2015).
- Hernandez Nava, A. et al. Reconciling early Deccan Traps CO_2 outgassing and pre-KPB global climate. *Proc. Natl Acad. Sci. USA* **118**, e2007797118 (2021).
- Svensen, H. et al. Hydrothermal venting of greenhouse gases triggering Early Jurassic global warming. *Earth Planet. Sci. Lett.* **256**, 554–566 (2007).
- Luttinen, A., Kurhila, M., Puttonen, R., Whitehouse, M. & Andersen, T. Periodicity of Karoo rift zone magmatism inferred from zircon

- ages of silicic rocks: implications for the origin and environmental impact of the large igneous province. *Gondwana Res.* **107**, 107–122 (2022).
6. Jiang, Q., Jourdan, F., Olierook, H. K. H. & Merle, R. E. An appraisal of the ages of Phanerozoic large igneous provinces. *Earth Sci. Rev.* **237**, 104314 (2023).
 7. Schoene, B., Eddy, M. P., Keller, C. B. & Samperton, K. M. An evaluation of Deccan Traps eruption rates using geochronologic data. *Geochronology* **3**, 181–198 (2021).
 8. Black, B. A., Karlstrom, L. & Mather, T. A. The life cycle of large igneous provinces. *Nat. Rev. Earth Environ.* **2**, 840–857 (2021).
 9. Heimdal, T. H., Godd eris, Y., Jones, M. T. & Svensen, H. H. Assessing the importance of thermogenic degassing from the Karoo Large Igneous Province (LIP) in driving Toarcian carbon cycle perturbations. *Nat. Commun.* **12**, 6221 (2021).
 10. Ullmann, C. V. et al. Warm afterglow from the Toarcian Oceanic Anoxic Event drives the success of deep-adapted brachiopods. *Sci. Rep.* **10**, 6549 (2020).
 11. Hilton, R. G. & West, A. J. Mountains, erosion and the carbon cycle. *Nat. Rev. Earth Environ.* **1**, 284–299 (2020).
 12. Storm, M. S. et al. Orbital pacing and secular evolution of the Early Jurassic carbon cycle. *Proc. Natl Acad. Sci. USA* **117**, 3974–3982 (2020).
 13. Penman, D. E., Caves Rugenstein, J. K., Ibarra, D. E. & Winnick, M. J. Silicate weathering as a feedback and forcing in Earth’s climate and carbon cycle. *Earth Sci. Rev.* **209**, 103298 (2020).
 14. John, C. M. et al. North American continental margin records of the Paleocene–Eocene thermal maximum: implications for global carbon and hydrological cycling. *Paleoceanography* **23**, PA2217 (2008).
 15. Sanei, H., Grasby, S. E. & Beauchamp, B. Latest Permian mercury anomalies. *Geology* **40**, 63–66 (2012).
 16. Pyle, D. M. & Mather, T. A. The importance of volcanic emissions for the global atmospheric mercury cycle. *Atmos. Environ.* **37**, 5115–5124 (2003).
 17. Thibodeau, A. M. et al. Mercury anomalies and the timing of biotic recovery following the end-Triassic mass extinction. *Nat. Commun.* **7**, 11147 (2016).
 18. Jenkyns, H. C. The Early Toarcian (Jurassic) anoxic event—stratigraphic, sedimentary, and geochemical evidence. *Am. J. Sci.* **288**, 101–151 (1988).
 19. Ruhl, M. et al. Astronomical constraints on the duration of the Early Jurassic Pliensbachian stage and global climatic fluctuations. *Earth Planet. Sci. Lett.* **455**, 149–165 (2016).
 20. Bodin, S. et al. More gaps than record! A new look at the Pliensbachian/Toarcian boundary event guided by coupled chemo-sequence stratigraphy. *Palaeogeogr. Palaeoclimatol. Palaeoecol.* **610**, 111344 (2022).
 21. Ruebsam, W. & Al-Husseini, M. Orbitally synchronized late Pliensbachian–early Toarcian glacio-eustatic and carbon-isotope cycles. *Palaeogeogr. Palaeoclimatol. Palaeoecol.* **577**, 110562 (2021).
 22. Wood, A. & Woodland, A. W. Borehole at Mochras, west of Llanbedr, Merionethshire. *Nature* **219**, 1352–1354 (1968).
 23. Scotese, C. R. An atlas of Phanerozoic paleogeographic maps: the seas come in and the seas go out. *Annu. Rev. Earth Planet. Sci.* **49**, 679–728 (2021).
 24. Xu, W. et al. Evolution of the Toarcian (Early Jurassic) carbon-cycle and global climatic controls on local sedimentary processes (Cardigan Bay Basin, UK). *Earth Planet. Sci. Lett.* **484**, 396–411 (2018).
 25. Woodland, A. W. (ed.). *The Llanbedr (Mochras Farm) Borehole Report No. 71/18* (Inst. Geol. Sci., 1971).
 26. Pieńkowski, G., Uchman, A., Ninard, K. & Hesselbo, S. P. Ichnology, sedimentology, and orbital cycles in the hemipelagic Early Jurassic Laurasian Seaway (Pliensbachian, Cardigan Bay Basin, UK). *Glob. Planet. Change* **207**, 103648 (2021).
 27. Percival, L. M. E. et al. Osmium isotope evidence for two pulses of increased continental weathering linked to Early Jurassic volcanism and climate change. *Geology* **44**, 759–762 (2016).
 28. Ullmann, C. V., Sz ics, D., Jiang, M., Hudson, A. J. L. & Hesselbo, S. P. Geochemistry of macrofossil, bulk rock and secondary calcite in the Early Jurassic strata of the Llanbedr (Mochras Farm) drill core, Cardigan Bay Basin, Wales, UK. *J. Geol. Soc.* **179**, jgs2021-018 (2022).
 29. Edwards, B. A., Kushner, D. S., Outridge, P. M. & Wang, F. Fifty years of volcanic mercury emission research: knowledge gaps and future directions. *Sci. Total Environ.* **757**, 143800 (2021).
 30. Percival, L. M. E. et al. Globally enhanced mercury deposition during the end-Pliensbachian extinction and Toarcian OAE: a link to the Karoo–Ferrar Large Igneous Province. *Earth Planet. Sci. Lett.* **428**, 267–280 (2015).
 31. Grasby, S. E., Them, T. R., Chen, Z., Yin, R. & Ardakani, O. H. Mercury as a proxy for volcanic emissions in the geologic record. *Earth Sci. Rev.* **196**, 102880 (2019).
 32. Font, E. et al. Rapid light carbon releases and increased aridity linked to Karoo–Ferrar magmatism during the early Toarcian oceanic anoxic event. *Sci. Rep.* **12**, 4342 (2022).
 33. Fantasia, A. et al. The Toarcian Oceanic Anoxic Event in southwestern Gondwana: an example from the Andean Basin, northern Chile. *J. Geol. Soc.* **175**, 883–902 (2018).
 34. Ruhl, M. et al. Reduced plate motion controlled timing of Early Jurassic Karoo–Ferrar large igneous province volcanism. *Sci. Adv.* **8**, eabo0866 (2022).
 35. Amos, H. M. et al. Global biogeochemical implications of mercury discharges from rivers and sediment burial. *Environ. Sci. Technol.* **48**, 9514–9522 (2014).
 36. Fendley, I. M. et al. Constraints on the volume and rate of Deccan Traps flood basalt eruptions using a combination of high-resolution terrestrial mercury records and geochemical box models. *Earth Planet. Sci. Lett.* **524**, 115721 (2019).
 37. Them, T. R. et al. Terrestrial sources as the primary delivery mechanism of mercury to the oceans across the Toarcian Oceanic Anoxic Event (Early Jurassic). *Earth Planet. Sci. Lett.* **507**, 62–72 (2019).
 38. Percival, L. M. E. et al. Does large igneous province volcanism always perturb the mercury cycle? Comparing the records of Oceanic Anoxic Event 2 and the end-Cretaceous to other Mesozoic events. *Am. J. Sci.* **318**, 799–860 (2018).
 39. DeVries, T. The ocean carbon cycle. *Annu. Rev. Environ. Resour.* **47**, 317–341 (2022).
 40. Vervoort, P., Adloff, M., Greene, S. E. & Turner, S. K. Negative carbon isotope excursions: an interpretive framework. *Environ. Res. Lett.* **14**, 085014 (2019).
 41. Sch ollhorn, I. et al. Pliensbachian environmental perturbations and their potential link with volcanic activity: Swiss and British geochemical records. *Sediment. Geol.* **406**, 105665 (2020).
 42. M uller, T. et al. Ocean acidification during the early Toarcian extinction event: evidence from boron isotopes in brachiopods. *Geology* **48**, 1184–1188 (2020).
 43. Smellie, J. L. in *Volcanism in Antarctica: 200 Million Years of Subduction, Rifting and Continental Break-up* (eds Smellie, J. L. et al.) Ch. 1.2 (Geological Society of London, 2021); <https://doi.org/10.1144/M55-2020-1>
 44. McElwain, J. C., Wade-Murphy, J. & Hesselbo, S. P. Changes in carbon dioxide during an oceanic anoxic event linked to intrusion into Gondwana coals. *Nature* **435**, 479–482 (2005).
 45. Jiang, Q. et al. Volume and rate of volcanic CO₂ emissions governed the severity of past environmental crises. *Proc. Natl Acad. Sci. USA* **119**, e2202039119 (2022).

46. Hesselbo, S. P. et al. in *Geologic Time Scale 2020* Vol. 2 (eds Gradstein, F. M., Ogg, J. G., Schmitz, M. D. & Ogg, G. M.) 955–1021 (Elsevier, 2020).
47. Al-Suwaidi, A. H. et al. New age constraints on the Lower Jurassic Pliensbachian–Toarcian boundary at Chacay Melehue (Neuquén Basin, Argentina). *Sci. Rep.* **12**, 4975 (2022).
48. Krause, A. J., Sluijs, A., van der Ploeg, R., Lenton, T. M., & Pogge von Strandmann, P. A. E. Enhanced clay formation key in sustaining the Middle Eocene Climatic Optimum. *Nat. Geosci.* **16**, 730–738 (2023).
49. Farnsworth, A. et al. Climate sensitivity on geological timescales controlled by nonlinear feedbacks and ocean circulation. *Geophys. Res. Lett.* **46**, 9880–9889 (2019).
50. Huang, Y., Fassbender, A. J. & Bushinsky, S. M. Biogenic carbon pool production maintains the Southern Ocean carbon sink. *Proc. Natl Acad. Sci. USA* **120**, e2217909120 (2023).
51. Salles, T. et al. Hundred million years of landscape dynamics from catchment to global scale. *Science* **379**, 918–923 (2023).
52. Deconinck, J., Hesselbo, S. P. & Pellenard, P. Climatic and sea-level control of Jurassic (Pliensbachian) clay mineral sedimentation in the Cardigan Bay Basin, Llanbedr (Mochras Farm) borehole, Wales. *Sedimentology* **66**, 2769–2783 (2019).
53. Bagnato, E. et al. Hg and CO₂ emissions from soil diffuse degassing and fumaroles at Furnas Volcano (São Miguel Island, Azores): gas flux and thermal energy output. *J. Geochem. Explor.* **190**, 39–57 (2018).
54. Capriolo, M. et al. Deep CO₂ in the end-Triassic Central Atlantic Magmatic Province. *Nat. Commun.* **11**, 1670 (2020).

Publisher's note Springer Nature remains neutral with regard to jurisdictional claims in published maps and institutional affiliations.

Open Access This article is licensed under a Creative Commons Attribution 4.0 International License, which permits use, sharing, adaptation, distribution and reproduction in any medium or format, as long as you give appropriate credit to the original author(s) and the source, provide a link to the Creative Commons licence, and indicate if changes were made. The images or other third party material in this article are included in the article's Creative Commons licence, unless indicated otherwise in a credit line to the material. If material is not included in the article's Creative Commons licence and your intended use is not permitted by statutory regulation or exceeds the permitted use, you will need to obtain permission directly from the copyright holder. To view a copy of this licence, visit <http://creativecommons.org/licenses/by/4.0/>.

© The Author(s) 2024

Methods

Mercury concentration

Mercury concentration was determined on powdered material using a Lumex RA-915M portable mercury analyser with Pyro 915+ attachment at the University of Oxford. The calibration curve was determined using aliquots of National Institute of Standards and Technology Standard Reference Material 2587 (Trace Elements in Soil Containing Lead from Paint, $\text{Hg} = 290 \pm 9 \text{ ng g}^{-1}$) of varying masses. Standards reproduced their accepted value within 5% on average. Sample duplicates ($n = 21$) were also analysed, and values were reproduced with an average percentage deviation of 11% and an average standard deviation of 1 ppb. We combine our new Hg dataset⁵⁵ with previously published Hg data from the Mochras core from refs. 27,30,32,34,38. The TOC and total inorganic carbon (TIC) data are reproduced here from refs. 12,24. TOC and TIC were determined using a Rock-Eval 6 (ref. 56). The CaCO_3 concentrations were then calculated from TIC ($\text{TIC} \times 8.333$), assuming TIC resides in CaCO_3 . Details of these analytical methods are available within the respective studies.

Data analysis

Our goal is to investigate the evolution of Hg deposition through time as a reflection of the changing availability of environmental mercury. Quantitative assessment of temporal variability in Hg loading of the environment is complicated by co-variation between Hg and other geochemical parameters such as TOC and sulfur (S) that can act as host phases for mercury in sediments³⁴. Although this co-variation is typically addressed via linear normalization by TOC (Hg is commonly associated with organic matter in the water column and in sediments deposited throughout geological history³¹), this approach does not always fully correct for host-phase biases and does not quantify how much additional Hg is present in excess of background levels during periods of Hg enhancement³¹ (Supplementary Information 1). We thus used a conceptual understanding of Hg sedimentary geochemistry to create a quantitative framework to calculate the amount by which the concentration of Hg in each sample deviates from the expected amount given the other chemical attributes of the sample (termed as residual Hg, Hg_R). This framework is based on an empirical assessment of the co-variation between Hg and other geochemical parameters (for example, concentration of TOC and S), including dilution effects due to sedimentary CaCO_3 —all of which are statistically significant in the Mochras dataset. The framework relies on the assumption that Hg behaves with consistent patterns throughout the dataset (which we demonstrate is true for our record; Supplementary Information 1.2) and thus requires a substantial dataset with a large proportion of ‘background’ periods without Hg-cycle perturbations.

The Hg_R is expressed in units of mass ratio (ng/g, ppb by mass). To calculate Hg_R , we first calculate calcium carbonate-free Hg and TOC (Hg_{cf} and TOC_{cf}) because Hg is most strongly correlated (inversely) with CaCO_3 in the Mochras dataset. Hg_{cf} does not co-vary statistically significantly with S_{cf} , but it does with TOC_{cf} . Hence, we use robust non-linear regression⁵⁷ to find a best-fit curve between Hg_{cf} and TOC_{cf} and calculate the residual (the distance from) to this curve for each sample (Supplementary Information 1). Robust regression (we use R package robustbase; see example code in Supplementary Information 6) is an optimal tool for fitting this curve since it weighs outliers less in the regression—outliers in Hg_{cf} versus TOC_{cf} most likely represent the presence of an additional Hg source that is not correlated with TOC. Robust nonlinear regression requires an initial choice of function for which the coefficients are found during regression. Here we find a hyperbolic tangent function to be the most useful as, with different coefficients, it can fit the range of curves that we frequently see in Hg versus TOC data, including quasi-linear co-variation. However, this choice is predicated on examining the behaviour present in each dataset as other functions may be appropriate in some cases (Supplementary Information 1).

There is no strong relationship between Hg_R and S, suggesting that, in this case, S is not a control on Hg concentration independent

of co-variation with TOC and hence does not need to be explicitly considered in the calculation of Hg_R . If a relationship between Hg_R (with respect to TOC_{cf}) and S_{cf} had been present, a second residual would have been calculated between these parameters, which would then accommodate variations in Hg driven by both TOC and S (as well as dilution by CaCO_3). However, Hg_R does not statistically significantly co-vary with TOC, CaCO_3 or S (or the equivalent CaCO_3 -free parameters), lending confidence that we have successfully removed the effects of dilution and host-phase abundance. We hypothesize that the residual Hg in this dataset represents an increase in the environmental abundance of Hg that is ultimately driven by activity associated with large-scale magmatism, considering the timescales involved ($\sim 10^3$ yr per sample). Other non-magmatic perturbations to the local or global environmental Hg load, such as recent Hg pollution from various industrial sources (unlikely to be relevant in the Mochras core record), might also be detected via this approach.

C emissions estimates and change in atmospheric p_{CO_2}

We estimate the CO_2 emissions (then converted to equivalent mass of carbon) that may have corresponded with the peaks in the sedimentary Hg record by first estimating Hg emissions using previously published Hg box-model results^{35,36} by scaling Hg enrichment to total Hg emission mass, assuming each point represents 1,000 years (consistent with a median sedimentation rate of -3.7 cm kyr^{-1} from our age model, sample size of a few centimetres, and Hg distribution over a few centimetres of sediment at time of deposition due to fluid infiltration). Then we use Hg/ CO_2 ratios from modern analogues to LIP degassing processes to estimate the CO_2 emissions that probably corresponded with the Hg emissions (Fig. 1). We present a range of Hg/ CO_2 ratios from 10^{-6} to 5×10^{-8} and hypothesize a middle-of-the-range ‘net’ Hg/ CO_2 ratio of 10^{-7} by mass (Figs. 1 and 3), spanning the majority of volcanic degassing measurements (eruptive and non-eruptive degassing) and estimates of thermogenic gases (Supplementary Information 4 and Supplementary Table 1)^{53,58–60}. We convert CO_2 emissions to equivalent C by mass fraction ($\text{C}/\text{CO}_2 = 12/44$ by mass).

Mercury has a shorter lifetime in the atmosphere and surface reservoirs (< 10 kyr) than CO_2 , which accumulates for 100s of kiloyears^{13,35}. We sum C emissions over 300 kyr rolling windows to approximate the timescale over which CO_2 accumulates until removed from the ocean–atmosphere system via silicate weathering (weathering releases cations, in particular Ca^{2+} , into the ocean, leading to the precipitation of carbonate minerals)¹³ and/or burial as organic carbon¹⁴. For comparison, see C emissions estimates with no rolling window in Supplementary Information 4.

To aid in comparison with the p_{CO_2} record and model results, we calculate the approximate final p_{CO_2} value following these emissions, assuming a constant initial p_{CO_2} of 500–1,000 ppm (consistent with the T-OAE p_{CO_2} record⁴²) using ocean/atmosphere equilibrium carbon-partitioning equations³⁹ (Supplementary Information 4). We plot the results of these equations, CO_2 release quantity versus p_{CO_2} increase, in Supplementary Information 4.

Data availability

All data generated or analysed during this study are included in this published paper (and its Supplementary Information) and are available at <https://doi.org/10.6084/m9.figshare.23301311>.

Code availability

The R script to calculate residual Hg for the Mochras dataset is available within the Supplementary Information.

References

- Fendley, I. et al. Early Jurassic large igneous province carbon emissions constrained by sedimentary mercury: dataset. *Figshare* <https://doi.org/10.6084/m9.figshare.23301311> (2024).

56. Behar, F., Beaumont, V. & Penteadó, H. L. D. B. Rock-Eval 6 technology: performances and developments. *Oil Gas. Sci. Technol.* **56**, 111–134 (2001).
57. Maechler, M. et al. R package ‘robustbase’: basic robust statistics, version 0.93-9. *R-Forge* (2021); <http://robustbase.r-forge.r-project.org/>
58. O’Keefe, J. M. K. et al. CO₂, CO, and Hg emissions from the Truman Shepherd and Ruth Mullins coal fires, eastern Kentucky, USA. *Sci. Total Environ.* **408**, 1628–1633 (2010).
59. Siegel, B. Z. & Siegel, S. M. in *Volcanism in Hawaii* (eds Decker, R. W., Wright, T. L. & Stauffer, P. H.) 825–839 (USGS, 1987).
60. Witt, M. L. I. et al. Mercury and halogen emissions from Masaya and Telica volcanoes, Nicaragua. *J. Geophys. Res. Solid Earth* **113**, B06203 (2008).

Acknowledgements

We thank S. Wyatt, O. Green and A. Paine (University of Oxford) for analytical assistance and J. Riding and S. Renshaw (British Geological Survey) for help with sample access. Thanks to A. Al-Suwaidi (Khalifa University) for discussion regarding KFLIP geochronology and C. Ullmann and R. Boyle (University of Exeter) for discussion of Mochras geochemistry and carbon cycle modelling. Funding was provided from an ERC Consolidator Grant (ERC-2018-COG-818717-V-ECHO) and a NERC large grant (NE/N018508/1 Integrated Understanding of the Early Jurassic Earth System and Timescale – JET).

Author contributions

I.M.F. analysed samples and designed statistical and Hg modelling methods. I.M.F., J.F. and T.A.M. analysed data and designed the study. M.R., S.P.H. and H.C.J. provided important background on Jurassic palaeoenvironment and aided in data analysis. I.M.F. wrote the paper with input from all authors.

Competing interests

The authors declare no competing interests.

Additional information

Supplementary information The online version contains supplementary material available at <https://doi.org/10.1038/s41561-024-01378-5>.

Correspondence and requests for materials should be addressed to Isabel M. Fendley.

Peer review information *Nature Geoscience* thanks Runsheng Yin and the other, anonymous, reviewer(s) for their contribution to the peer review of this work. Primary Handling Editor: Alison Hunt, in collaboration with the *Nature Geoscience* team.

Reprints and permissions information is available at www.nature.com/reprints.